Pre-print Paper 8th International Conference of Engineering Against Failure (ICEAF-VIII), Kalamata, Greece, June 22nd-25th, 2025

Automated Defect Recognition and Property Prediction based on Non-Destructive Evaluation of High Pressure Die Cast (HPDC) Samples based on primary and partially secondary AlSi10MnMg Alloys †

Stefan Bosse [1,*], Dirk Lehmhus [2], Marco Haesche [2], Leonardo Fernandes Gomes [2], Charlotte Graner [3]

[1] Department & Institute of Computer Science, University of Koblenz, Universitätsstraße 1, 56070 Koblenz, Germany; sbosse@uni-koblenz.de

[2] Department of Casting Technologies, Fraunhofer Institute for Manufacturing Technology and Advanced Materials IFAM, Wiener Straße 12, 28359 Bremen, Germany; dirk.lehmhus@ifam.fraunhofer.de (D. L.), marco.haesche@ifam.fraunhofer.de (M.H.), leonardo.fernandes.gomes@ifam.fraunhofer.de (L. F. G.)

[3] Fraunhofer Institute for Material and Beam Technology, Winterbergstraße 28, 01277 Dresden, Germany; charlotte.graner@iws.fraunhofer.de (C. G.)

* Correspondence: sbosse@uni-koblenz.de; Tel.: (49)261 287-2723

† Presented at the 8th International Conference of Engineering Against Failure (ICEAF-VIII), Kalamata, Greece, June 22nd-25th, 2025.

Abstract: The present study investigates the possibility of using AI methods to identify and characterize defect populations in thin-walled HPDC samples using data from non-destructive testing (NDT), considering specifically X-ray radioscopy and ultrasonic evaluation. Automated Defect Recognition (ADR) and statistical characterization are enhanced using synthetic training data and the results compared to an evaluation based on pre-defined class-limiting samples. Beyond ADR, the focus is on prediction of failure characteristics based on the acquired NDT data. HPDC samples cover three different variants representing the AlSi10MnMg family of alloys, one of them a primary material, the others containing 58 wt.-% and 89 wt.-% of secondary materials, respectively.

Keywords: Non-Destructive Testing (NDT); Automated Defect Recognition (ADR); mechanical properties; aluminum; primary materials; secondary materials; metal casting;

1. Introduction

The advent of e-mobility has started to shift the larger part of the carbon footprint associated with the life cycle of passenger cars from the use phase to production. While the battery still accounts for a large part of carbon dioxide emissions, the body in white is second in line according to several studies. At the same time, a general trend towards increased use of cast aluminum components for structural applications has raised the contribution of this material, and in terms of manufacturing processes, of high pressure die casting (HPDC). This development has already been described by the HPDC

Citation: To be added.

equipment manufacturer Bühler in 2019 [1], but it received a further boost when Tesla introduced the GigaCasting concept just one year later [2]. Combined, both tendencies more than compensate the loss of traditional cast powertrain components like engine block, cylinder head, gearbox or oil pan [3]. The drawback is that on a global average, primary aluminum carries a considerable burden in terms of CO_2 emissions: Typical figures for the year 2022 range from 5.3 t CO_2/t Al for production in Europe versus 12.7 t CO_2/t Al for production in China [4]. In contrast, remelting post-consumer scrap accounts for as little as 0.5 t CO_2 / t Al [5]. So why not use only secondary aluminum in automotive body manufacture? The problem is twofold – for one thing, the growing use of aluminum in the automotive industry contributes to the fact that secondary aluminum is scarce, and cannot easily be sourced from other industries, as they tend to have their recycling chains and networks already in place. Besides, the demand in terms of alloys for structural parts does not match what is on offer from powertrain components: Available materials tend to have e.g. higher content levels of elements like copper, iron, zinc or manganese. As a consequence, there is a considerable body of literature by now which focuses on analyzing the impact of such accumulations on material characteristics like castability, mechanical strength or corrosion resistance [6,7,8]. The present paper adds another perspective: We compare a primary alloy with two nominally similar alloys featuring different levels of secondary material content – however, we do not only look at composition, but also at defects: Do these come out differently in primary and secondary alloys, and do they affect mechanical characteristics differently? We base these evaluations on visual inspection of X-ray radioscopy images of samples to identify four different quality level classes, an Automated Defect Recognition (ADR) approach applied to a more detailed set of radioscopy images [9], and high-frequency ultrasonic testing results. In addition, we conducted tensile tests to evaluate the relative performance of samples and correlate them with the observed quality data and defects. Part of the activities in this respect were facilitated by the Fraunhofer Society's "FutureCarProduction" project which is dedicated to the parallel evaluation of sustainability, performance and cost of automotive body structure material and process solutions in early stages of the design process [10,11].

2. Materials and Methods

2.1. Materials

Three different alloys were compared in this study, all of them conforming to the specification of an AlSi10MnMg casting alloy in accordance with the alloy designation EN AC-43500, DIN EN 1706:2021-10 [12]. One of these alloys was entirely based on primary materials (Silafont-36®, Aluminium Rheinfelden Alloys GmbH, Rheinfelden, Germany), while two others contained 58 wt.-% (Aluminium Rheinfelden Alloys GmbH, Rheinfelden, Germany) and 89 wt.-% (SILVAL-10®, Raffmetal S.p.a., Casto, Italy) of secondary aluminum. The exact composition of these alloys in the as received state is given in Table 1. Prior to casting, Mg and Sr content levels were adjusted to approximately 0.27 wt.-% and 0.023 wt.-%, respectively, in all alloys to improve comparability.

Table 1. Composition of the alloys compared in the experiments: Supplier specifications and analyses of the actual batches used in the experiments as provided by the suppliers.

Alloy	Element content level [wt.-%]														
	Si	**Fe**	**Cu**	**Mn**	**Mg**	**Cr**	**Zn**	**Ti**	**Sr**	**Ni**	**Pb**	**Sn**	**Sb**	**Ca**	**P**
Silafont-36® specification*	9.5-11.5	<0.15	<0.03	0.5-0.8	0.1-0.5	-	<0.07	0.04-0.15	0.010-0.025	-	-	-	-	-	<0.001
Silafont-36® 100 wt.-% primary**	10.28	0.082	0.002	0.513	0.146	0.001	0.001	0.008	0.002	-	-	-	-	-	-
AlSi10MnMg 58 wt.-% secondary**	10.18	0.13	0.02	0.61	0.27	0	0.01	0.06	0.0171	0.009	0.002	0.0006	0.002	-	-
SILVAL-10® Specification*	9.0-11.5	<0.35	<0.05	0.40-0.6	0.15-0.40	-	<0.1	<0.15	opt.	<0.05	-	-	-	-	-
SILVAL-10® 89 wt.-% secondary**	9.95	0.338	0.023	0.471	0.279	0.011	0.026	0.075	0.0275	0.007	0.005	0.001	0	0.0009	0.001

* Supplier's specification. For Silafont-36®, maximum amount of elements for which no explicit limit is given is 0.10 wt.-%. For SILVAL-10®, the respective value is 0.15 wt.-%, which no individual element surpassing a threshold of 0.05 wt.-%.

** Supplier's analysis of the actual batches used in the present experiments.

2.2. Methods

To assess specimens we need different quantitative and qualitative measures. The porosity analysis is central. In [13] the authors compared different measuring methods to assess the porosity of die casted specimens. They conclude that X-ray Computed Tomography (CT) and radioscopy are suitable methods to get an accurate measure of the porosity, but outline the limited usability of Ultrasonic testing. X-ray CT provides 3-dim. characterization of single pores, whereas X-ray radioscopy provides statistical characterization of pore distributions. The methodological metric used in this work and the data flow is shown in Figure 1, the methods are discussed in the next Sections.

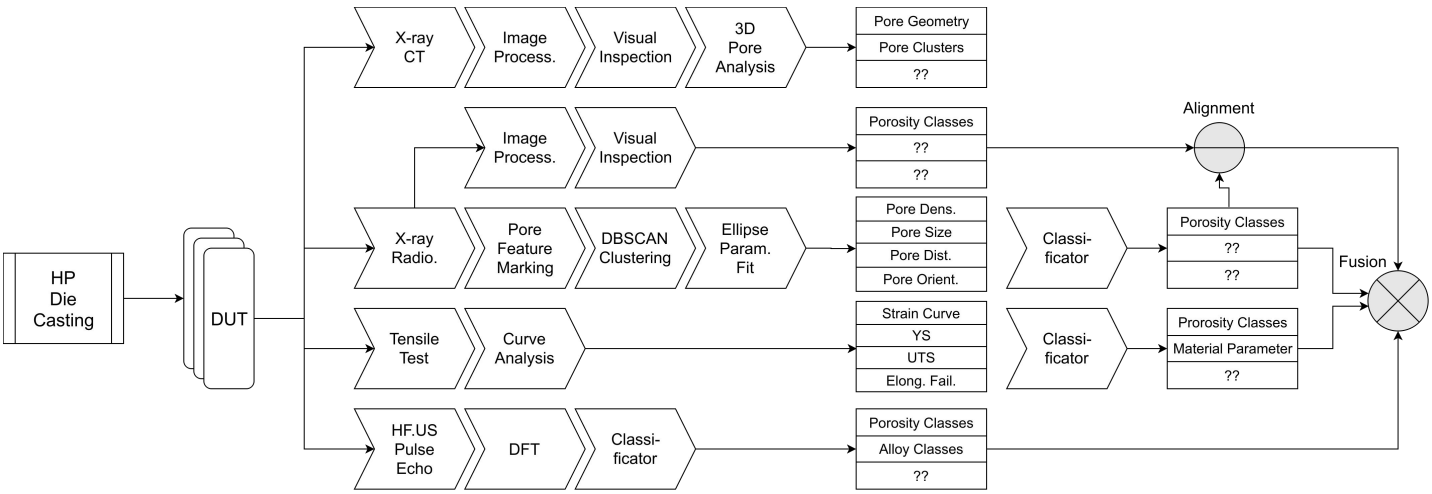

Figure 1. Overview of the methods and the data flow used in this work.

2.2.1. High Pressure Die Casting

Samples were produced by means of high pressure die casting using a Frech DAK 250 HPDC machine with a locking force of 290 t. The melt temperature in the holding furnace was set to 710 ± 10°C, while the die temperature was controlled at a level of 190 ± °C. The plunger velocity was set at 3.8 m/s during the second, filling phase, which corresponds to a velocity at the in-gates of approximately 51.20 m/s. The die used provides a rectangular bending test samples as well as a tensile test geometry as depicted in Figure 2.

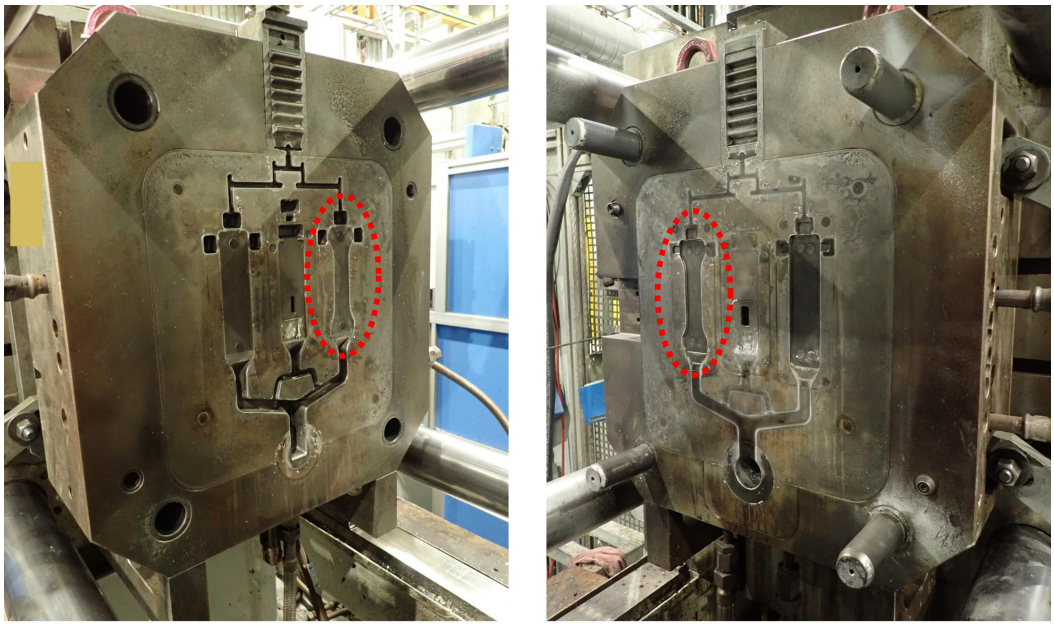

Figure 2. HPDC die used for samples production: (a) movable side and (b) fixed side. The cavity from which the samples used in the present study is highlighted in red.

The present study is focused on the dogbone-type tensile test samples. Thickness of the samples is 3 mm. Table 1 outlines the numbers and types of samples produced during the test campaign as well as the investigations performed on them. For subjective classification based on limiting samples, X-ray images of all samples were taken (for details, see section 3.2.2) for categorization as A, B, C or D quality level.

Table 2. Overview of the number of samples cast and numbers used for the various investigations.

Number and use of samples	**AlSi10MnMg 100 wt.-% primary**	**AlSi10MnMg 58 wt.-% secondary**	**AlSi10MnMg 89 wt.-% secondary**
Total number of samples	198	100	130
Visual classification based on X-ray radioscopy (IFAM)	198	100	130
ADR of porosity based on X-ray radioscopy with a micro-focus X-ray tube (University of Koblenz)	18	14	18
Pulse-echo HF US (University of	18	14	18

Koblenz)			
Tensile testing (Fraunhofer IWS)[1]	15 (4A/3B/3C)	15 (4A/3B/4C)	11 (3A/4B/4C)

[1] Tensile tests were performed on 5 samples per alloy variant and quality class, however, in some cases, failure occurred not within the test length L_o: These samples were not considered in the further evaluation. The actual number of samples evaluated per alloy and quality level is given in brackets.

2.2.2. X-ray Radioscopy

X-ray radioscopy was performed both at Fraunhofer IFAM and at University of Koblenz. At Fraunhofer IFAM, an Yxlon MU-2000 unit (Comet Yxlon GmbH, Hamburg, Germany) was used for image acquisition. The respective data is used for establishing initial quality classes based on visual inspection. X-ray µ-focus radioscopy performed by the University of Koblenz is used to get a quantitative measure of the planar projection of material porosity by using an automated feature marking ML approach combined with point clustering (ADR), as introduced in previous work [9]. The pore feature marking model was trained with synthetic X-ray images derived by X-ray simulation and geometric modeling (providing ground-truth data). µX-ray CT was used to measure pore characteristics used for the synthetic data generation. Input of the ADR system is an X-ray image acquired with an X-ray tube providing a sufficiently small Focal Spot Diameter (in this work with a FSD of 35µm), output is a feature marking overlay image discriminating pixels belonging to a pore from noise. The feature marking image is processed by a pixel clusterer (DBSCAN), subsequently applying pixel groups to a hull computation and ellipse fitting. The ADR thus delivers statistics of pore and pore size distributions (average pore diameter, pore area, pore density, average pore orientation etc.). The X-ray radioscopy systems capture images with a solid-state, X-ray image intensifier, or camera-screen device. The typical geometrical projection magnification was about two.

2.2.3. Ultrasonic Testing

X-ray radiography is an expensive test method and requires special treatment and care. To simplify the estimation of the material porosity we evaluate in this work the usability of broadband high-frequency pulse-echo ultrasound monitoring. We used a dual piezo-crystal transducer with a center frequency of 5 MHz and a diameter of 10 mm (no-name brand, originally intended for material thickness measurement). We measured the material response signal with a Gaussian-windowed sine burst (sine wave base frequency 5 MHz, 500ns duration) as well as with a bipolar short pulse (100ns). In [14,15] the authors evaluated the relationship between material porosity and the frequency-dependent attenuation of Ultrasonic waves, which should here deployed to predict the porosity class as introduced in Section 3. The stimulus signal was generated with an Arbitrary Wave Generator (AWG), GWInstek AWG-125, and the response signal was captured with a Digital Storage Oscillopscope (DSO), Owon VDA 1022. An industrial coupling gel for ultrasound thickness transducers was used to attach the transducer to the specimen surface. The used double-piezo transducer is not a broad-band transducer, but is characterized by a series of resonance frequencies in a range extending from 1 to 6 MHz, which is assumed to be a suitable approximation.

The down-sampled frequency spectrum (with 100 frequency points) calculated with a Fast Fourier Transform (FFT) from the echo signal was used as the input for a data-driven classification model (e.g., a simple two-layer Artificial Neural Network) to estimate the porosity class as identified by X-ray testing.

2.2.4. Mechanical Testing

Quasistatic mechanical testing was performed on selected samples covering all alloy variants and all quality classes using a Inspect Table 50 kN universal testing system equipped with a video extensometer of type ONE1-M5 (Hegewald & Peschke Meß- und Prüftechnik GmbH, Nossen, Germany). Pre-loading was done at a test speed of 4 mm/min, followed by 0.6 mm/min up to the yield point and 16.08 mm/min until failure.

3. Results and Discussion

Analysis of X-ray data was based on inspection of X-ray radioscopy images. Four different quality classes were distinguished, with samples differentiated from Class A (best quality) to Class D (lowest quality). Samples in the fourth category (Class D) were considered rejects and were not subjected to further testing. Figure 3 depicts typical examples of samples belonging to quality classes A to D. Images were transformed to binary state using image editing software (GIMP 3.0.4) to highlight the differences. Classification itself was based on the original images. Figure 4 shows results of the manual classification of samples.

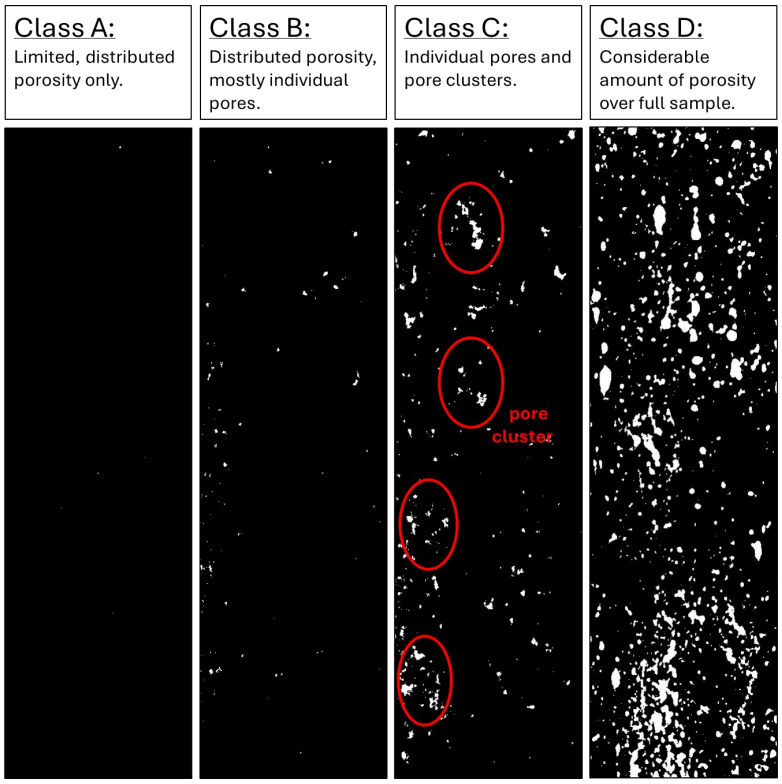

Figure 3. Exemplary depiction of binarized X-ray images representing the four quality classes A, B, C and D (rejects) distinguished in visual inspection.

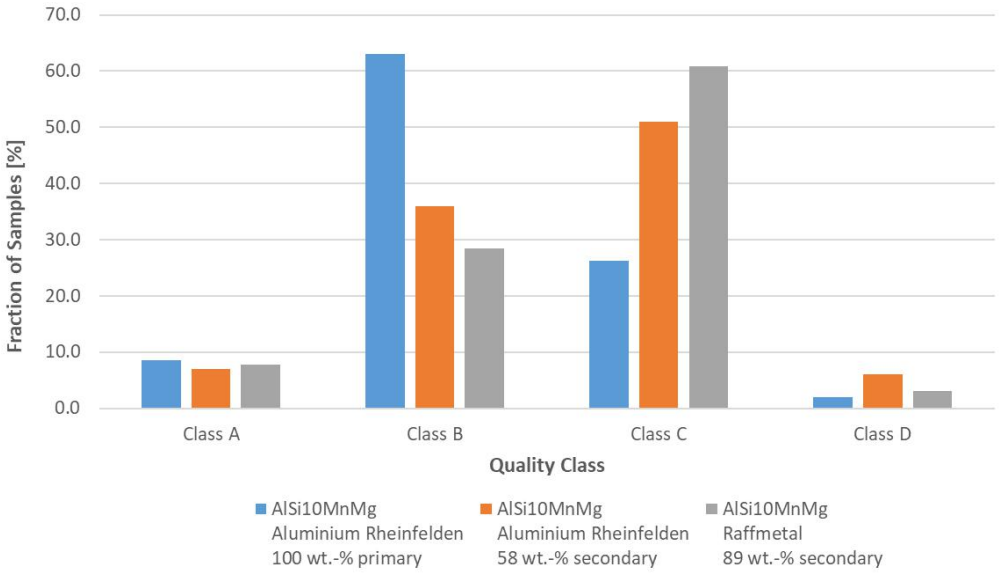

Figure 4. Results of the manual classification of samples: Fraction of samples in each quality class for the primary and the two partially secondary alloys.

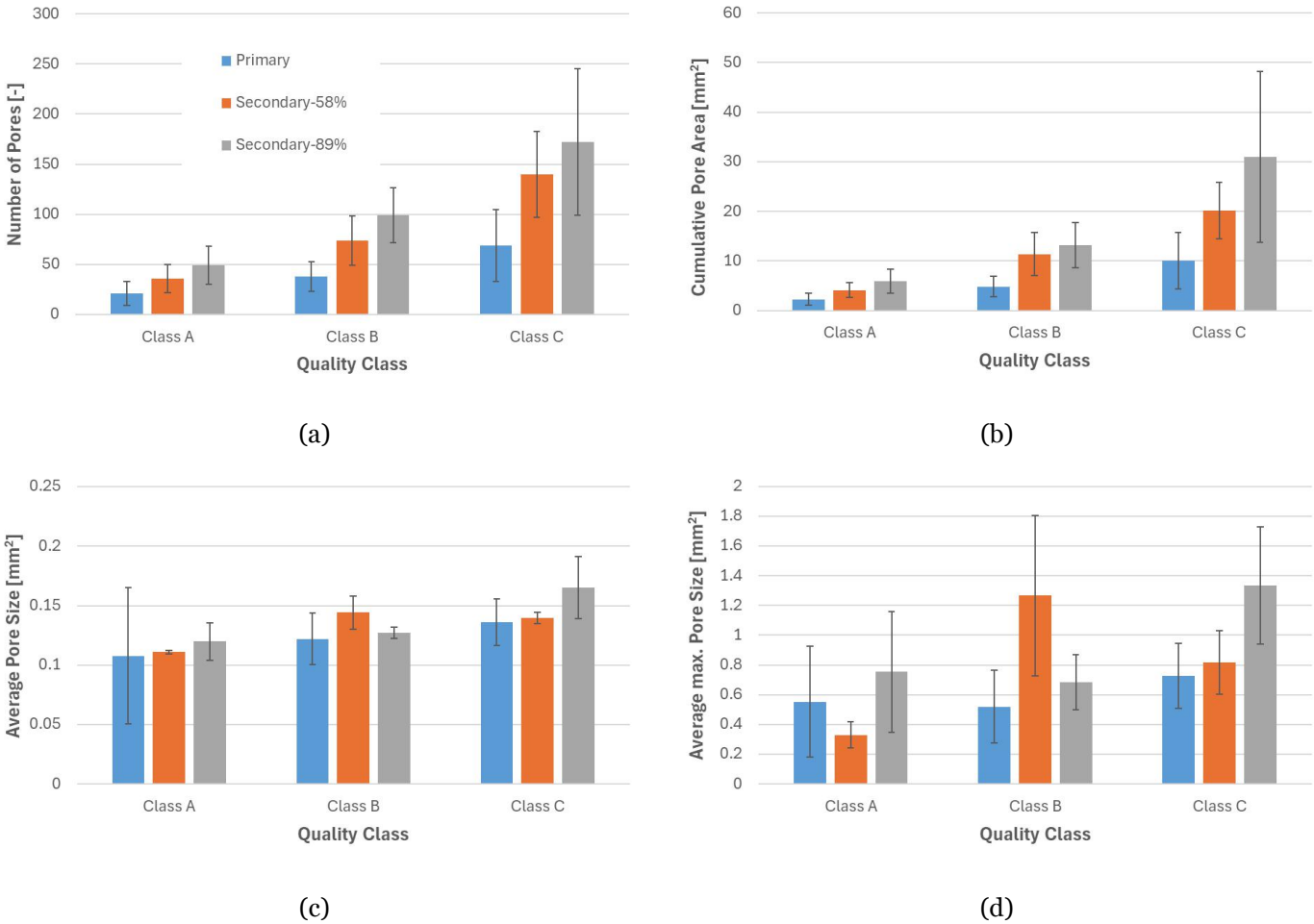

Figure 5. Overview of ADR results: (a), number of pores, (b) cumulative pore area, (c) average pore size and (d), average maximum pore size for all alloy variants and quality classes. All diagrams show values averaged over several samples for the respective class. The error bars reflect the standard deviation.

X-ray radioscopy ADR data for the different materials and quality classes confirms the distinction between quality classes. An overview is provided in Figure 5, focusing on number of pores, accumulated pore area, average pore size and maximum pore size. Tensile test data is summarized in Figure 6. As mentioned above, class D samples were not considered for tensile testing. Note that the thickness of the tensile test samples matches that of the actual castings, which is 3 mm.

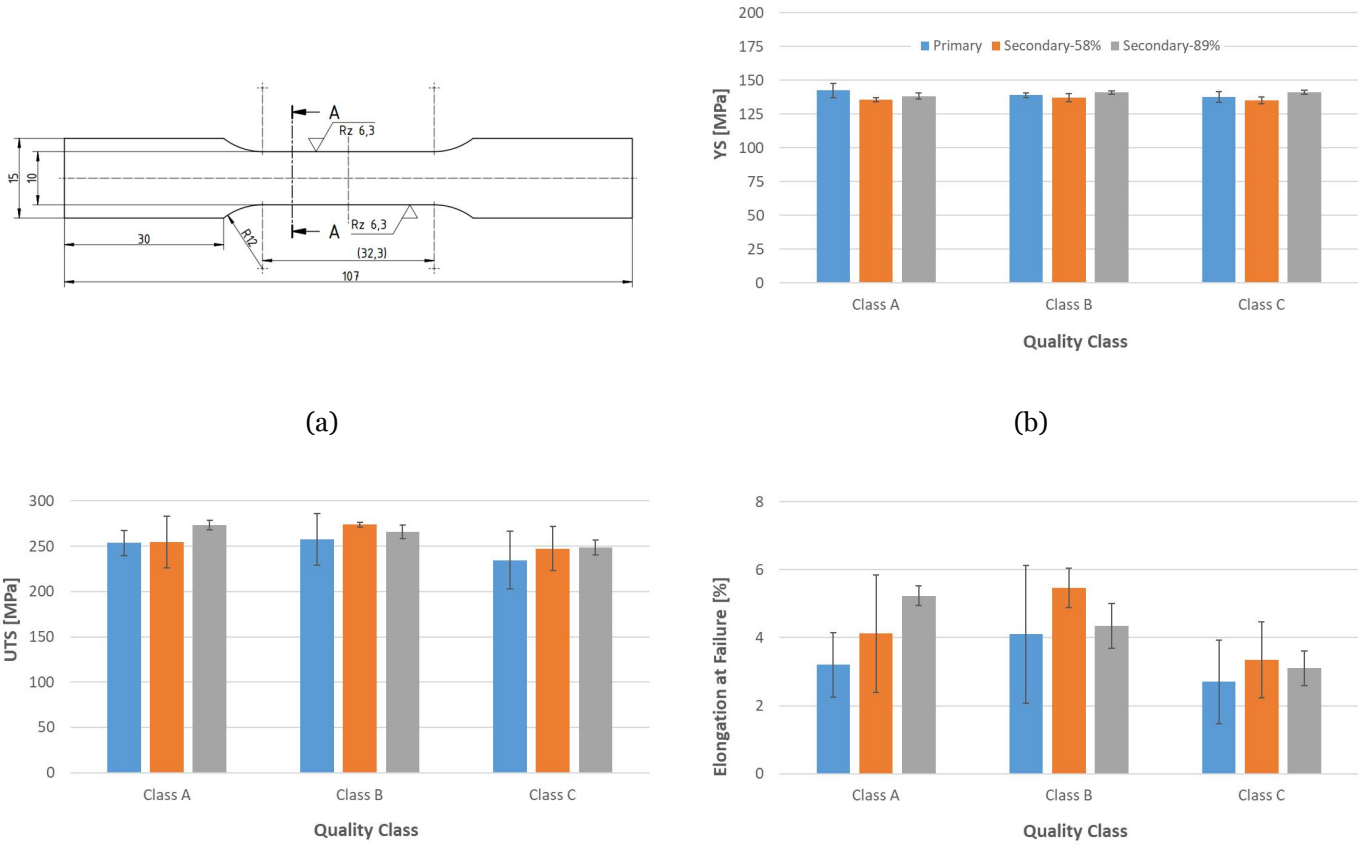

Figure 6. Tensile test results an accompanying information: (a), geometry and dimensions of the tensile test sample as cut from the cast samples, (b) Yield Strength (YS), (c) Ultimate Tensile Strength (UTS) and (d), elongation at failure for all alloy variants and quality classes.

Comparison of the tensile strength data reveals no significant deviation between primary and secondary alloys. In fact, the alloy containing 89 wt.-% recycled material exhibits highest UTS levels at class A quality. What is more, in terms of yield strength, the differences between the three top quality classes accepted for tensile testing are marginal irrespective of the alloy.

The ultimate tensile strength data matches elongation at failure in terms of the general tendencies. When looking at both for the primary and the 58 wt.-% secondary alloy, both characteristics increase from class A to class B, but drop to the lowest level for class C. At first sight, this might be assumed to indicate that there is no measurable effect of porosity on strength, however, it is more likely that the transition from class B to class C marks the level and distribution of porosity, as well as size of pores, from which porosity actually becomes relevant with respect to affecting the mechanical properties.

The close relation between UTS and elongation at failure becomes obvious when looking at the stress-strain curves recorded. Again, irrespective of alloy and quality class, all show a strictly increasing shape and no peak level, which would otherwise denote the boundary between global an localized plastic deformation. Since thus no necking occurs, a lower elongation at failure must necessarily coincide with a lower UTS value.

In general, all materials tested fell short of the specification data for both Silafont-36® and SILVAL-10® in terms of elongation at failure, while both yield strength and ultimate tensile strength staid within the specified range in the case of the primary alloy and the one containing 58 wt.-% of secondary material. In contrast, while reaching the specification level in terms of yield strength, the 89 wt.-% secondary alloy undercut the ultimate tensile strength value by a margin of approximately 6%, even though the actual values surpassed those determined for the other two alloys. Table 3 summarizes this data and compares it to the values measured on class A samples in the present test campaign (standard deviation added in brackets). However, a further distinction must still be made between yield strength and ultimate tensile strength, as the former tends to be in the upper half of the specified levels, while the latter either just about meets this requirement, or falls short of it as discussed above. A possible explanation of this observation is an accumulation of detrimental phases in the alloy containing the highest amount of recycled materials, which could limit elongation to failure, cutting the stress-strain curve short before reaching a maximum and thus also limiting the UTS value. However, the observation that it is explicitly this material which shows the highest levels of elongation at failure would not entirely fit this rationalization. In general, when plotting the elongation at failure against ultimate tensile strength, there is an identical tendency for all alloy variants and all quality levels according to which the highest elongation at failure coincides with the highest ultimate tensile strength levels. This can be seen as a reflection of premature failure of the alloys prior to reaching their actual limits in terms of plastic deformation. Since the primary alloy does not outperform those with secondary material content, and quality classes are not distinguished either with respect to the general trend, it may be assumed that individual distributions of porosity as well as types of defects not detectable using the methods employed here control the observed effect.

Table 3. Overview of the number of samples cast and numbers used for the various investigations.

Source of Data	**YS [MPa]**	**UTS [Mpa]**	**Elongation at failure [%]**
Specification Silafont-36®, F state [16][1]	120-150	250-290	5-11
Test data Silafont-36® (100 wt.-% primary)[2]	142.5 (5.26)	253.75 (13.82)	3.2 (0.94)
Test data AlSi10MnMg (58 wt.-% secondary)[2]	135.75 (1.50)	254.5 (28.38)	4.13 (1.73)
Specification SILVAL-10®, F state [17][1]	125	290	6
Test data SILVAL-10® (89 wt.-% secondary)[2]	138.3 (2.08)	273.3 (5.51)	5.23 (0.29)

[1] Specification data for HPDC, as cast condition (F state). Both Aluminium Rheinfelden and Raffmetal assume 3 mm wall thickness, matching conditions in our own experiments.

[2] Class A samples considered exclusively.

It is possible that the mechanical properties shown here are not only affected by porosity, but also by other types of defects. Oxide inclusions as well as oxide biofilms are examples of this kind which can typically not be detected by means of radioscopy [18,19,20], but which may still have a major effect – an effect which, according to some authors, dominates porosity in terms of controlling ductility and strength for HPDC parts [21].

Comparison of the frequency spectra of the pulse-echo ultrasound signal data, as shown in Figure 7, reveals significant differences between primary and secondary alloys given by the amplitude ratio of the two main peaks. The primary alloy has a peak ratio of 1:1 for the 5.5 and 4.5 MHz peaks, whereas the secondary alloys show a peak ratio of about 2 for the sek-58 and about 1.5 for the sek-89 alloy. But there is no obviously visible significant difference in the spectra of the two secondary alloys. To investigate a potential hidden correlation between the porosity classes (A-C) we applied a simple functional ML model (ANN) to the down-samples spectral signal data. The ANN consists of two layers and [10,5] sigmoid-activated neuronal nodes and a final softmax layer with three outputs, one for each class A,B, and C, respectively. The model was trained using the adam optimizer and a batch size of 5 samples. The entire data set consists of 150 ultrasound signals from 50 specimens measured at three positions along the long axis of the specimen. The data set was split into 80/20% training/test data partitions. The training data was augmented by applying normal distributed multiplicative noise within the range [0.6,1.4], in total about 500 augmented training samples. Only the augmented data was used for the training consisting of 1000 epochs and a termination condition of 2% classification error (average computed during the training).

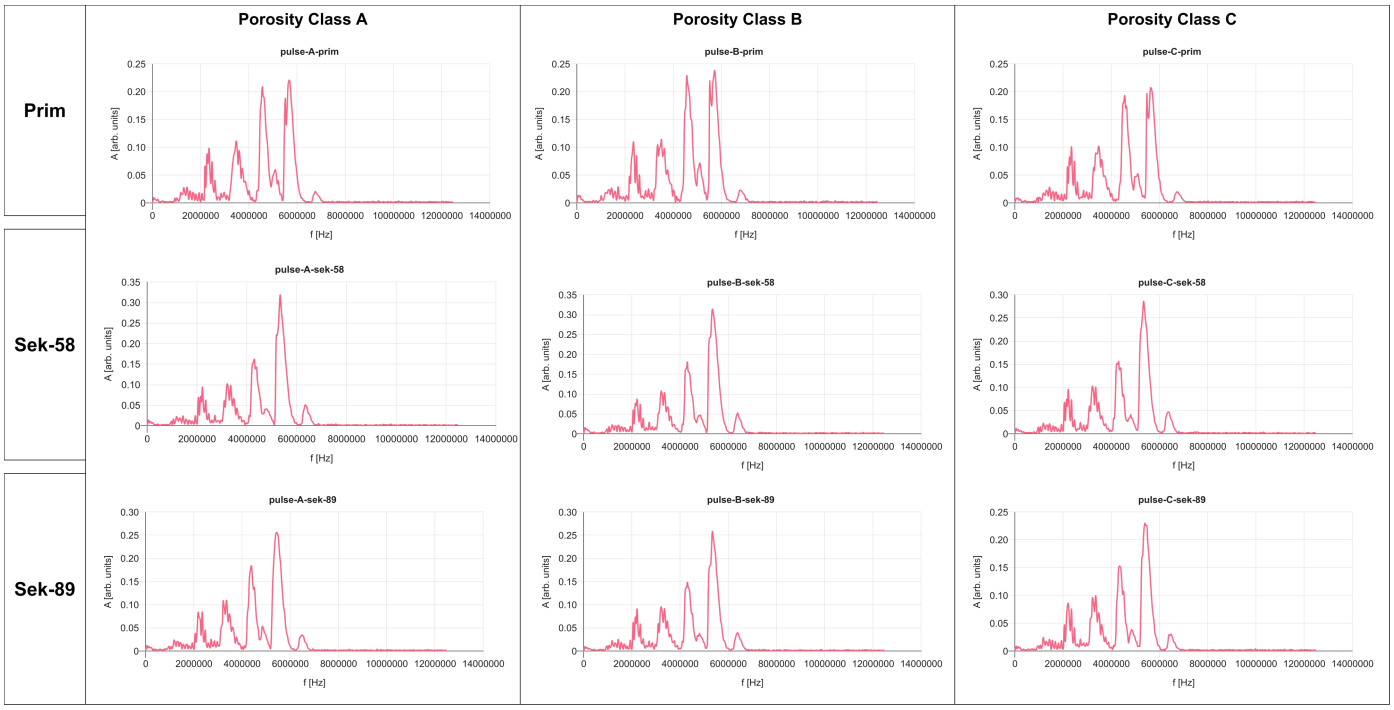

Figure 7. Averaged frequency spectra of hf-ultrasound pulse-echo measurements for three different porosity classes (A,B,C) and alloys (prim, sek-58, sek-89. The primary alloys can be clearly distinguished from the sek-nn alloys by the peak ratio of the two main peaks. The non-continuous frequency spectra are a result of transducer resonances and not related to material properties. A spectral dependency of the spectra from the porosity class cannot be identified.

Although the training process converges fast and smoothly with a final low classification error of the original signal data (in the range of 0-5%), the prediction on any randomly selected test data (not contained in the training data set) still yields a high classification error of about 20-40%, below the guessing probability, but compared to the error of the training data results a clear indicator for a highly specialized predictor model. Due to the limited number of specimens available in each alloy class we cannot split the prediction process into three (or at least two) separate models for each alloy class.

One major issue with US pulse-echo monitoring is the limited detection area (around 15 mm²) and the inhomogeneous distribution of pores as shown in the example images in Figure 3. The low average correlation between the class prediction and the US signal data can be a result of this low detection coverage.

4. Conclusion

Separation of samples in four different quality classes via visual inspection of radioscopy images was largely confirmed by the ADR data, with the exception that the limiting values derived from the latter separating two classes differed significantly depending on the alloy variant. For example, primary alloy samples classified as B quality showed lower or matching numbers of pores and accumulated pore area compared to secondary alloy samples sorted into the A category, indicating that class limits were stricter in the case of the primary alloy. The same tendency was observed for the material variant containing 58 wt.-% secondary alloy compared to the one with 89 wt.-% secondary aluminum.

In contrast, tensile test data does not fully reflect the quality levels established based on X-ray data. Yield strength levels are almost identical for all material variants and all quality classes, and all fall within the specification ranges for the Rheinfelden and the Raffmetal alloy. Ultimate tensile strength was found to be highest for the Raffmetal material with the highest level of recycled content. Other than the two other alloys, the Raffmetal alloy also showed a distinctive reduction both in UTS and elongation at failure values from quality class A to C. Such a clear trend was not observed for the other two alloys, however, a possible explanation beyond the limited number of samples is that the distinction between class A and class B chosen here was too fine, and only the larger amount and clustering of pores observed in class C started to affect mechanical properties. However, this assumption would have to be confirmed e.g. by a deeper analysis of the fracture surfaces of the tensile test samples to rule out the possibility that other classes of defects like oxide inclusions or oxide biofilms affected failure in some way not accounted for by the X-ray and ultrasound investigations, which could not be expected to detect oxide biofilms specifically. However, the ultrasound signals can be used to distinguish primary and secondary alloys with high confidence. The signal spectra show only weak correlation with the porosity, which can be exploited by a data-driven classification model, but with a low degree of generalization (results are very specific to the specimens). Possible causes can be an inhomogeneous pore distribution in conjunction with a small detection area and the spectra dependency on the alloy composition. Further investigations on the ultrasound signal analysis should be carried out, e.g., by using time-frequency space features and wavelet transformation, as well as an analysis of explainability of ML models used to predict material characteristics to avoid any specialized analysis system.

Author Contributions: Conceptualization, S.B. and D.L.; methodology, S.B., D.L. and C.G.; software, S.B.; validation, S.B.; formal analysis, S.B., D.L., C.G., L.F.G; investigation, S.B., D.L., M.H., L.F.G. and C.G.; resources, S.B. and D.L.; data curation, S.B.; writing—original draft

preparation, D.L. and S.B.; writing—review and editing, S.B., M.H.; L.F.G. and C.G.; visualization, D.L. and S.B.; supervision, S.B. and D.L.; project administration, S.B. and D.L.; funding acquisition, D.L. All authors have read and agreed to the published version of the manuscript.

Funding: Part of this research was funded by the Fraunhofer Gesellschaft zur Förderung der Angewandten Forschung e.V. within the framework of the Fraunhofer Flagship Project "FutureCarProduction – comprehensive approaches for the evaluation and development of integral car body concepts for sustainable vehicle manufacturing" (project ID 38330, https://www.fraunhofer.de/en/research/lighthouse-projects-fraunhofer-initiatives/fraunhofer-lighthouse-projects/future-car-production.html).

Abbreviations

The following abbreviations are used in this manuscript:

ADR	Automated Defect Recognition (using ML and image processing)
ANN	Artificial Neural Network
DIN EN	Deutsches Institut für Normung / Europäische Norm
EN AC	European Norm / Aluminum Casting
FFT	Fast Fourier Transform
HF	High Frequency
HPDC	High Pressure Die Casting
NDT	Non-Destructive Testing
US	Ultrasound / Ultrasonic
UTS	Ultimate Tensile Strength
YS	Yield Strength

References

1. Roos, H. J.; Lagler, M.; Quintana, L. Whitepaper: The Future of Structural Components in HPDC (Bühler AG, Uzwil, Switzerland, 2019). Available online: https://dam.buhlergroup.com/asset/d81f1241f84448e09399c2520c8218a3 (accessed on September 5th, 2025).
2. Tesla Reportedly Makes One-Piece Giga Casting Breakthrough, https://insideevs.com/news/686793/tesla-reportedly-makes-one-piece-giga-casting-breakthrough, accessed on-line 15.9.2025
3. Lehmhus, D. Advances in Metal Casting Technology: A Review of State of the Art, Challenges and Trends – Part I: Changing Markets, Changing Products. *Metals* **2022**, *12*, 1959, doi:10.3390/met12111959.
4. Cleanest And Dirtiest Countries for Primary Aluminum Production. Available online: https://www.globalefficiencyintel.com/new-blog/2022/cleanest-and-dirtiest-countries-for-primary-aluminum-production (Accessed on September 2nd, 2025)
5. Hydro CIRCAL – Premium recycled aluminium with minimum 75% post-consumer scrap. Available online: https://www.hydro.com/en/global/aluminium/products/low-carbon-and-recycled-aluminium/low-carbon-aluminium/hydro-circal/ (Accessed on September 5th, 2025)
6. Cinkilic, E.; Moodispaw, M.; Zhang, J.; Miao, J.; Luo, A. A. A New Recycled Al-Si-Mg Alloy for Sustainable Structural Die Casting Applications. *Metallurgical and Materials Transactions A* **2022**, *53A*, 2861-2873, doi:10.1007/s11661-022-06711-4.

7. Nunes, H.; Emadinia, O.; Soares, R.; Vieira, M. F.; Reis, A. Adding Valuer to Secondary Aluminum Casting Alloys: A Review on Trends and Achievements. *Materials* **2023**, *16(3)*, 895, doi:10.3390/ma16030895.

8. Balasubramani, N.; Moodispaw, M.; Luo, A. A. Controlling the Fe-intermetallic phases and mechanical properties of secondary Al-9Si-1Fe alloy with Cr and Mn additions. *Journal of Materials Science & Technology* **2025**, *206*, 135-152.

9. Bosse, S.; Lehmhus, D.; Kumar, S. Automated Porosity Characterization for Aluminum Die Casting Materials Using X-ray Radiography, Synthetic X-ray Data Augmentation by Simulation, and Machine Learning. *Sensors* **2024**, *24(9)*, 2933, doi: 10.3390/s24092933.

10. Rohwer, V.; Krinke, S.; Lehmhus, D.; Pille, C.; Fendt, D. Sustainable Materials in Automotive Body Engineering – The Role of (Giga-) Casting Technology to Meet Net Zero Targets. In Proceedings of the 2024 NADCA Congress & Exposition, Indianapolis, Indiana, USA, September 30th - October 2nd, 2024.

11. Bleicher, C.; Qaralleh, A.; Lehmhus, D.; Haesche, M.; Fernandes Gomes, L.; Pintore, M.; Kleinhans, R.; Sommer, S.; Tlatlik, J. Aspects for the Optimization of Car Production Regarding Efficiency, Availability and Sustainability. *SAE Technical Paper* **2025**, 2025-01-8609, doi:10.4271/2025-01-8609.

12. Aluminium and aluminium alloys – Castings - Chemical composition and mechanical properties. German Standard DIN EN 1706:2021-10. Beuth Verlag: Berlin, Germany, 2021; https://dx.doi.org/10.31030/3283422

13. Wilczek, Aneta, Piotr Długosz, and Marek Hebda: Porosity characterization of aluminium castings by using particular non-destructive techniques. Journal of Nondestructive Evaluation 34.3 (2015): 26.

14. Adler, Laszlo, and Shaio-Wen Wang: Ultrasonic measurement of porosity in casts and welds. NASA. Lewis Research Center Analytical Ultrasonics in Materials Research and Testing (1986).

15. Hillger, Wolfgang, S. Elze, and Bremen Airbus: Determination of porosity of aerospace structures by ultrasonic pulse echo technique. CD: 8th ECNDT Barcelona 2002 (2002): 1-7.

16. Silafont. Available online: https://rheinfelden-alloys.eu/legierungen/silafont/ (accessed September 5th, 2025)

17. Material data sheet – Alloy group: AlSi10Mg – Alloy designation: SILVAL-10®. Revision 3, December 2023. Raffmetal S. p. a., Casto, Italy.

18. Campbell, J. An Overview of the Effects of Bifilms on the Structure and Properties of Cast Alloys. *Metallurgical and Materials Transactions B* **2006**, *37B*, 857-863.

19. Gopalan, R.; Prabhu, N. K. Oxide bifilms in aluminium alloy castings – a review. *Materials Science and Technology* **2011**, *27(12)*, 1757-1769.

20. Hu, M.-L.; Yang, K.-Y.; Chang, W.-J.; Deng, B.; Luo, J.-T.; Guo, H.-M. Bifilm Defects in AlSi10MgMn Alloy Castings.

21. Olofsson, J., Bogdanoff, T.; Tiryakioğlu, M. On the Competition between Pores and Hidden Entrainment Damage during In Situ Tensile Testing of Cast Aluminum Alloy Components. *Metals* **2024**, *14*, 1175.